



A simple scaling model for balling defect formation during laser powder bed fusion

Viktor Lindström^a, Giandomenico Lupo^a, Jian Yang^a, Vladyslav Turlo^a,
Christian Leinenbach^{a,b,*}

^a Empa, Swiss Federal Laboratories for Materials Science and Technology, Ueberlandstrasse 129, 8600 Dübendorf, Switzerland

^b Laboratory for Photonic Materials and Characterization, École Polytechnique Fédérale de Lausanne, 1015 Lausanne, Switzerland

ARTICLE INFO

Keywords:

Laser powder bed fusion
Balling
Lack-of-fusion
Computational fluid dynamics
Defect prediction

ABSTRACT

Balling is one of the cornerstone defects in laser powder bed fusion of metals, leading to high porosity of the 3D printed parts and substantially deteriorating their performance. The transition to the balling mode is commonly identified through a series of trial-and-error experiments, an extremely inefficient approach. Here, we propose an outstandingly simple thermal scaling model for predicting the threshold from balling mode to conduction mode in laser powder bed fusion. The resulting balling criterion can be expressed as a dimensionless number which combines the material properties, the powder size and the pre-heating of the substrate. The model predictions are well in agreement with our validation experiments for three different materials (copper, bronze and steel). The applicability of the model assumptions is verified through a set of suitably designed multiphysics computational fluid dynamics simulations. The combination of first-hand experiments and simulations substantiates the balling model as a readily usable and reliable scaling criterion for establishing the minimum required power for laser powder bed fusion, applicable to different materials, as well as suggesting viable strategies to adjust the operating parameters towards the defect-free regime.

1. Introduction

In recent years, Laser Powder Bed Fusion (LPBF) of metals has evolved from a mere prototyping technology to a manufacturing technology for the fabrication of parts with intricate 3D geometries and new functionalities. Their quality with regard to processing defects such as pores and cracks is of high importance, and a thorough understanding of the defect formation mechanisms is required for the reliable fabrication of such parts.

In this context, analytical and semi-analytical models are useful for describing various aspects of LPBF. Scaling analyses are particularly important, because they provide relations for process operation that are applicable to different materials and processing parameters.

Hann et al. [1] first introduced a thermal scaling for predicting the size of laser-welding melt pools, by defining a scaling parameter, called normalized enthalpy, which relates the laser energy density, the laser dwell time, the thermal diffusion time of the metal, and the melt pool enthalpy. King et al. [2] and Rubenchik et al. [3] have applied similar scaling laws for collapsing the melt pool characteristic size in

LPBF-processing onto a single master curve, independent of the material properties and processing parameters. Ye et al. [4] also showed that the fraction of the laser energy input that is absorbed by the powder bed is, to a good approximation, a function of the normalized enthalpy.

King et al. [2] have also used the same scaling law to predict the threshold from conduction mode to keyhole mode. This transition is often accompanied by the formation of pores, as shown by high-speed imaging and Computational Fluid Dynamics (CFD) simulations [5], [6]. Ghasemi-Tabasi et al. [7] showed that the keyhole transition can be transferred from one material to another using the normalized enthalpy as a scaling parameter.

A different model for predicting the presence of defects in conduction mode LPBF has been presented by Tang et al. [8]. This model uses a geometrical assumption of the shape of the melt pool to predict the presence of gaps in-between the hatches and layers of successive scans. The model only requires one parameter, the width of the melt-pool, which can be calculated by a simple approximation of the thermal field, as given by Mirkoohi et al. [9].

A defect that has become increasingly important with the growing interest in LPBF of copper [10] and precious metals [11] is the so-called

* Corresponding author at: Empa, Swiss Federal Laboratories for Materials Science and Technology, Ueberlandstrasse 129, 8600 Dübendorf, Switzerland.
E-mail address: christian.leinenbach@empa.ch (C. Leinenbach).

Nomenclature			
A_{cap}	cross-sectional area	S_D	dampening D'Arcy force
A_{cell}	area of the patch	S_E	evaporative cooling
A_{wetted}	wetted area	S_L	volumetric laser heat source
a	characteristic length of laser beam	S_L^{cell}	volumetric laser heat source of cell
Ba	balling number	S_R	force for recoil pressure
c_p	heat capacity	S_σ	force for surface tension
c_p^g	heat capacity of gas	T	temperature
c_p^l	heat capacity of liquid	T_0	initial temperature of the substrate
c_{pL}	heat capacity of liquid	T_L	liquidus temperature
c_p^m	heat capacity of mushy zone	T_M	melting temperature
c_p^s	heat capacity of solid	T_S	solidus temperature
DC	proportionality coefficient	T_V	boiling temperature
d	direction of the laser	u	fluid velocity field
d_L	characteristic length	u	scanning speed
d_{new}	updated laser direction	u_L	characteristic liquid velocity in the melt pool
d_{old}	old laser direction	V	volume of melt track
e	eccentricity	V_{cell}	volume of cell
f	fraction of the absorbed energy going into heating and melting the powder	x	coordinate
h	cap height	z	coordinate
I	integral	z_{norm}	normalized coordinate
J_i	Bessel functions	α	optical absorption coefficient
k	thermal conductivity	α_{eff}	effective absorptivity of the powder bed
k_G	thermal conductivity of gas	γ	fraction of liquid metal to the total metal
k_L	thermal conductivity of liquid	ΔT_M	temperature difference
k_S	thermal conductivity of solid	δ	fraction of power reaching the solid substrate
L_{fus}	latent heat of fusion	ϵ	small number
L_{vap}	latent heat of vaporization	Θ	normalized temperature
M	molar mass of the metal	θ	contact angle of wetting
n	interface normal	κ	surface curvature
n	number of nearest neighbor lines	λ	dummy variable
P	laser power	λ'	substitution variable
$P_{balling}$	minimum laser power required to avoid balling	μ	viscosity
Pe	thermal Péclet number	μ_{gas}	gas viscosity
$P_{particle}$	power of generated particle	μ_L	liquid viscosity
$P_{particle,initial}$	initial power of generated particle	μ_{metal}	metal viscosity
p	pressure	μ_S	solid viscosity
p_0	surrounding thermodynamic pressure	σ_{LG}	temperature dependent surface tension coefficient
r_s	circle segment radius	ρ	density
R	universal gas constant	ρ_G	gas density
r_{norm}	normalized coordinate	ρ_L	liquid density
r	coordinate	ρ_{metal}	metal density
r_l	laser spot radius	τ_{cond}	heat diffusion time scale
r_p	particle radius	τ_{slosh}	average time scale between the eccentricity peaks or troughs
r_w	wetting radius	ϕ	phase fraction of metal
		ψ	non-dimensional number
		ψ^*	non-dimensional number

balling porosity,¹ which is illustrated in Fig. 1. Several mechanisms for balling have been proposed for different processing conditions:

- At high laser scanning velocities, hydro-dynamic capillary instabilities have been proposed by Gu and Shen [12] and Li et al. [13]

¹ The terms "incomplete melting" and "lack-of-fusion pores" are often used synonymously to balling pores, but in this paper they are distinguished. Incomplete melting is defined as when the powder layer is not completely molten, as shown in Fig. 1(a) on the left. Balling is defined as pores due to poor wetting. This is defined as when the contact angle, θ , is greater than 90°. Lack-of-fusion pores are defined as the type of defects occurring in conduction mode ($\theta < 90^\circ$).

as a potential mechanism for balling. Such a mechanism has been explained using an analytical stability criterion and observed in numerical simulations [14], when the melt pool is elongated enough for the onset of instabilities of the Plateau-Rayleigh type [15]. However, this mechanism is unlikely to explain the observed balling in precious metals and copper, where the temperature distribution and melt pool shape can be expected to be hemispherical due to the high thermal conductivity [3].

- For alloys forming surface oxides, Li et al. [13] showed that an oxygen content of the order of 10% by volume in the surrounding gas can lead to balling due to poor wettability of the molten metal on the oxide. On the other hand, experiments with gold alloys and copper alloys have shown a reduction of lack of fusion porosity when

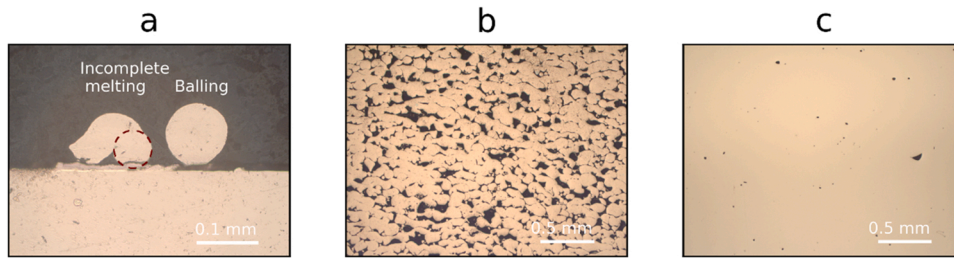


Fig. 1. (a) Cross-sections of single laser scans of pure copper on a copper substrate showing the difference between incomplete melting and balling. The original size of the unmolten powder particle is visible on the left, and marked with the dashed line. The gap between the substrate and weld tracks occurs on cooling of the sample after embedding it in hot plastic. (b) Cross-sectioned sample of LPBF-processed Cu-Sn alloy exhibiting porosity (black areas) due to balling. The ball like shapes are significantly larger than the powder diameter. (c) Lack-of-fusion porosity in a part made from

stainless steel.

oxidizing the surface of the feedstock powder, due to the reduced reflectivity of the oxidized surface [15–17].

- For a loose powder bed without solid support (overhang LPBF), Gu and Shen [12] observed that too high power density can lead to balling, due to the numerous hot spots that drive the Marangoni flow, which are formed because the melt pool tends to get overheated as dissipation through powder surface point contacts is inefficient. This phenomenon has later been confirmed by effective medium and CFD simulations by King et al. [14]. These conditions are however not representative of the conditions in the majority of LPBF-parts, where balling is observed.
- Klocke and Wagner [18] suggested that balling defects might occur if the time available for coagulation of the powder particles is too short before solidification occurs. Statistical analysis performed by Mao et al. [19] on a copper-tin alloy however shows that the defect formation is not significantly dependent on the scanning speed, in the range that they considered.

Different approaches were proposed to alleviate balling defects. Numerous studies, for example by Mao et al. [19] and Jadhav et al. [17], proved that increasing the power (for copper well above 500 W) decreases balling. Klotz et al. [16] showed that another possible strategy to decrease balling porosity in gold alloys is to alloy the feedstock powder with elements like germanium, titanium, and iron to decrease the thermal conductivity. It has been further shown by Lindström et al. [20], Jadhav et al. [21] and Gu and Shen [12] that increasing the powder absorptivity or pre-heating the substrate are effective strategies. However, the relative influence of these parameters is not well understood, making it difficult to evaluate which strategy is the best for a given application.

In this work, an analytical scaling criterion for predicting the threshold from balling mode to conduction mode in LPBF at low to moderate laser scanning speeds is proposed, based on a suggested balling mechanism that considers the thermal balance between the molten powder and the solid surface. The validity of the analytical model assumptions is verified by CFD simulations, and the model applicability for different materials is demonstrated by LPBF experiments using copper, bronze and steel powder as feedstock.

2. Model description

2.1. The temperature field in balling mode

As the laser spot travels over the powder bed, with scanning speed u , it induces melting of one or more powder particles. Heat accumulates inside the powder particles because it releases to the substrate slowly through a narrow point contact, leading to temperatures well above the melting temperature of the material. The molten particles will, as shown by numerical simulations by Khairallah et al. [5], start wetting their neighbors, which will start melting as well and agglomerate into one cohesive melt due to the surface tension of the liquid metal. Once the molten powder starts wetting the surface of the previously consolidated

layer, the heat transfer to the substrate will gradually increase. The total laser power will partly be reflected, partly be consumed by the heating and melting of the powder, and partly constitute heat losses due to evaporation and radiative cooling [5]. Finally, as shown in Fig. 2, the leftover heat will be transferred to the substrate in an approximately uniform manner through the solid-liquid interface, corresponding to the thermal boundary condition of the substrate:

$$\left. \frac{\partial T}{\partial z} \right|_{z=0} = \begin{cases} \frac{P\delta}{A_{\text{wetted}}k}, & \text{wetted surface} \\ 0, & \text{non-wetted surface} \end{cases} \quad (1)$$

where T is the temperature, z the direction normal to the solid-liquid interface which is assumed to be the substrate surface at the very beginning of wetting, A_{wetted} the wetted area, P the total laser power, δ the fraction of power that reaches the solid substrate, and k the thermal conductivity of the solid substrate. It should be mentioned that this simplified model neglects the flow in the molten metal, as well as the temperature and phase dependence of the physical and transport properties (such as thermal conductivity, density, and heat capacity). In the frame of reference of the moving laser with scanning speed u following x direction and at steady state, the temperature field in the heat-affected zone is governed by the following heat equation:

$$0 = -u\rho c_p \frac{\partial T}{\partial x} + k\nabla^2 T, \quad (2)$$

where ρ is the density and c_p the heat capacity of the solid substrate.

We further assume that the scanning speed u is low compared to the thermal diffusivity, as indicated by the ratio $\psi < 1$, where ψ is expressed

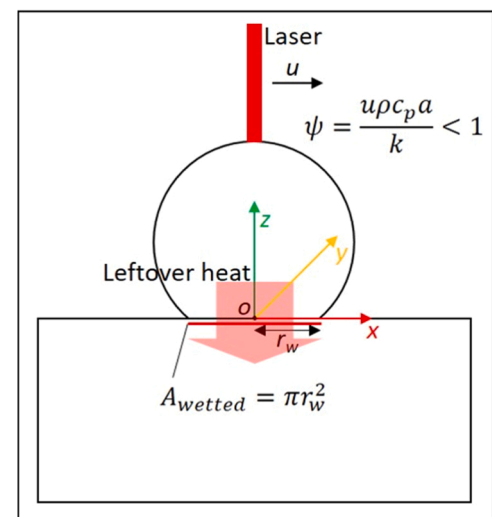


Fig. 2. Schematic for the simplified heat transfer problem corresponding to Eqs. (1)–(6).

as:

$$\psi = \frac{u\rho c_p a}{k} \quad (3)$$

where a is the characteristic length scale of the laser beam, usually chosen to be the $1/e^2$ laser radius. The non-dimensional number ψ , which we introduce, is similar in form to the thermal Péclet number but it represents the ratio of the thermal diffusion time to the laser dwell time, and it corresponds to the inverse of the parameter p introduced by Rubenchik et al. [3]. This assumption corresponds to quasi-steady heat transfer in the absolute frame of reference, and it is realistic for metals like copper, gold, and silver, with high thermal conductivity, where the ψ ratio is around 0.2 for a scanning speed of 300 mm/s. In that case, the heat transfer expressed by Eq. (2) is dominated by thermal conduction, thus, the first term, $-u\rho c_p \frac{\partial T}{\partial x}$, becomes negligible compared to the second term, $k\nabla^2 T$. Eq. (2) then reduces to Laplace's equation:

$$0 = \nabla^2 T \quad (4)$$

Assuming a circular contact area of radius r_w (the wetting radius) between the molten cap and the substrate, the boundary condition of the substrate can be easily described in cylindrical coordinates (the origin and z axis coincide with ones shown in Fig. 2):

$$\left. \frac{\partial T}{\partial z} \right|_{z=0} = \begin{cases} \frac{P\delta}{\pi r_w^2 k}, & |r| \leq r_w \\ 0, & |r| > r_w \end{cases} \quad (5)$$

According to Carslaw and Jaeger [22], Eqs. (4) and (5) have an analytical solution in the cylindrical coordinates, in terms of Bessel functions of the first kind, J_i :

$$T(r, z) = \frac{P\delta}{\pi r_w k} \int_0^\infty \frac{e^{-\lambda|z|} J_0(\lambda r) J_1(\lambda r_w)}{\lambda} d\lambda + T_0 \quad (6)$$

where r is the radial distance from the center and T_0 the initial temperature of the substrate. Note that λ is a dummy variable, which disappears upon calculation of the integral.

As the liquid spreads over the solid surface, heat is dissipated in the substrate at an increasing rate due to the increased contact area. As the wetting of a liquid metal on its own substrate is almost perfect, the molten powder would in principle be able to spread over the complete substrate. However at some point the temperature in the melt close to the triple line separating the liquid, solid and gas phases, $T(r_w, 0)$, will reach the melting temperature, T_M , and solidification of the cap will begin, thereby hindering any further spreading of the melt.

To find the point where spreading stops, we set $T_M = T(r_w, 0)$ in Eq. (6), which with the substitution $\lambda' = \lambda r_w$ leads to:

$$T_M = T(r_w, 0) = \frac{P\delta}{\pi r_w k} \int_0^\infty \frac{J_0(\lambda') J_1(\lambda')}{\lambda'} d\lambda' + T_0 = \frac{P\delta}{\pi r_w k} I + T_0 \quad (7)$$

The numerical value of the integral, I , is approximately 0.64. Setting $\Delta T_M = T_M - T_0$ we get the equilibrium wetting radius:

$$r_w = I \frac{P\delta}{\pi \Delta T_M k} \quad (8)$$

2.2. The shape of the cap

Since we neglect the molten metal flow, the molten cap is constrained by the wetting radius given by Eq. (8), i.e. the molten metal does not overflow, and the shape of the cap is geometrically determined by the wetting radius r_w and the volume of molten metal along the track. For the sake of simplicity, we assume that the powder layer consists only of spherical powder grains with one well-defined particle radius, r_p , and that the powder is densely packed. For a melt track along a symmetry axis of the powder layer the powder particle line density will be $1+2n$

powder grains per powder diameter, where n is the number of nearest neighbor lines that have been coagulated into the melt, Fig. 3(a). We assume that the melt has the form of an extruded circle segment, Fig. 3(b). The relevant dimensions of the cap cross section are the cap height h , wetting radius r_w , circle segment radius r_s , and contact angle θ , as specified in Fig. 3(c).

The volume of the melt track is given by the cross-sectional area, A_{cap} , multiplied by the track length. According to Fig. 3(b), this volume must be equal to the volume of the coagulated particles along the melt track:

$$V = 2r_p \cdot A_{cap} = (1+2n) \frac{4}{3} \pi r_p^3 \quad (9)$$

The resulting equation for the cross-sectional area is thus:

$$A_{cap} = (1+2n) \frac{2\pi}{3} r_p^2 \quad (10)$$

The area is that of a circular section:

$$A_{cap} = \frac{r_s^2}{2} (2\theta - \sin(2\theta)) \quad (11)$$

and the following relations also hold:

$$r_w = r_s \sin(\theta) \quad (12)$$

$$r_s = \frac{h}{2} + \frac{r_w^2}{8h} \quad (13)$$

By numerically solving Eqs. (10)-(13) for a given value of n and a given wetting radius, the radius R , contact angle θ , and height h , are obtained.

The solution of Eqs. (10)-(13) is illustrated in Fig. 4 where the values of θ and h are shown as a function of r_w for $n = 1, 2$ and 3 , with the distances normalized by r_p . Balling pores will form if $\theta > 90^\circ$ due to the formation of voids between the individual caps when they solidify. For $n = 1$, the criterion is fulfilled when $r_w \approx 2r_p$. A slight fluctuation of the wetting width would however cause the cap to touch the powder particles in the next line ($n = 2$), causing them to coagulate into the melt (see Fig. 4(a)). This would cause the volume of molten material to increase, which in turn would lead to $\theta > 90^\circ$. For $n = 2$ the fluctuation would have to be significantly larger to touch the powder belonging to line $n = 3$.

Balling pores will therefore be avoided when $\theta < 90^\circ$ for $n = 2$. As can be seen in Fig. 4(a) this corresponds to $r_w \approx 2.6r_p$, or larger. When this occurs, the height of the cap will still be higher than the original powder layer (see Fig. 4(b)). This could possibly lead to pores forming due to the uneven shape of the layer. Thus, processing parameters should probably be chosen so that the wetting width is larger than $3.7r_p$, in order to keep the cap height smaller than $2r_p$ as seen in Fig. 3(b) for $n = 2$. It is important to note that in the expressions above the relevant powder radius is the largest powder radius in the distribution since the stochastic nature of the powder delivery will at some point bring a cluster of these close together, possibly leading to the formation of a pore.

2.3. The balling criterion: combining the temperature field with the cap shape

Combining the criterion for balling, $r_w = 2.6r_p$ with Eq. (8) results in the minimum laser power required to avoid balling porosities:

$$P_{balling} = \pi \cdot \frac{2.6}{I} \frac{r_p k \Delta T_M}{\delta} = 12.8 \frac{r_p k \Delta T_M}{\delta} \quad (14)$$

It can be seen from Eq. (14) that available strategies for mitigating balling defects by reducing the balling power threshold can be the reduction of the powder size r_p relative to the laser spot, the pre-heating of the substrate (i.e. reducing ΔT_M), or the increase of δ , which could

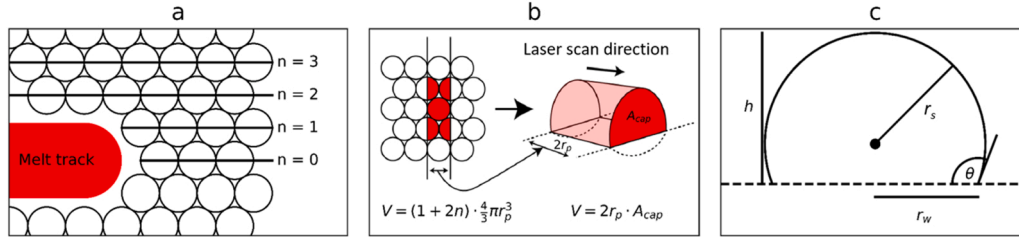


Fig. 3. (a) Melting of densely packed powder and wetting on a substrate. The number of wetted neighbor lines, n , is 1. (b) The volume of the molten powder is equivalent to the volume of the cap. (c) Schematic cross-section of the cap with the relevant parameters.

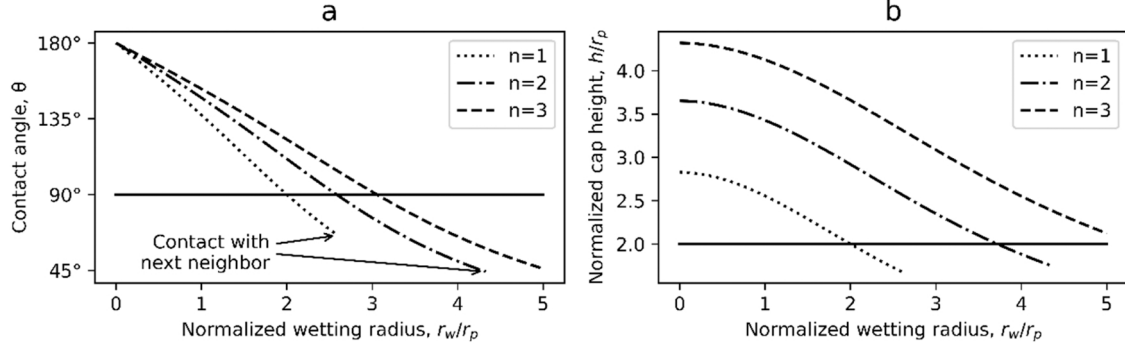


Fig. 4. The parameters of the cap as a function of the wetting radius calculated from Eqs. (10)–(13) with $n = \{1, 2, 3\}$. a) Contact angle, θ , with the balling criterion $\theta = 90^\circ$ marked. b) Cap height, h , with the solid line marking the point when the cap height is lower than the powder diameter. All distances are normalized by the powder radius.

theoretically be achieved by changing the morphology of the powder bed using e.g. the particle size distribution.

A convenient way of expressing the power threshold for balling is as a dimensionless input power from here on referred to as the balling ratio:

$$Ba = P/P_{balling} \quad (15)$$

This number expresses how close the processing parameters are to the balling threshold, and it must be bigger than unity to ensure that no balling occurs.

Under the model assumptions, the balling ratio completely determines the temperature field in the substrate. This can be seen by normalizing the temperature field of Eq. (6) by the balling threshold power of Eq. (14) and rearranging it in dimensionless form (details are presented in [supplementary material 1](#)):

$$\Theta(r_{norm}, z_{norm}) = I^{-1} \int_0^\infty \frac{e^{-\lambda' |z| \frac{3}{2.6Ba}} J_0(\lambda' r_{norm} \frac{1}{2.6Ba}) J_1(\lambda')}{\lambda'} d\lambda' \quad (16)$$

where the normalized temperature is given by $\Theta(r_{norm}, z_{norm}) = \frac{T(r, z) - T_0}{T_M - T_0}$, and the normalized coordinates are $r_{norm} = r/r_p$ and $z_{norm} = z/r_p$.

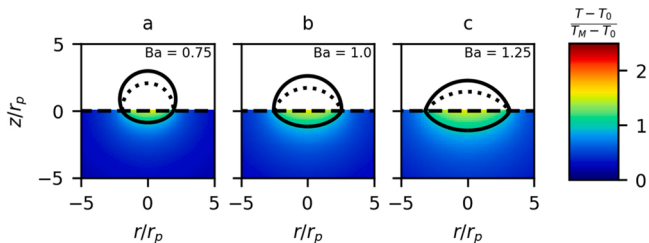


Fig. 5. The normalized temperature field of a single track calculated from Eq. (16) and the corresponding cap with $n = 1$ (dotted line) and $n = 2$ (solid line). a) Below the balling threshold, $Ba = 0.75$. b) At the balling threshold, $Ba = 1.0$. c) Above the balling threshold, $Ba = 1.25$.

In Fig. 5, the normalized temperature field is shown, below, at, and above the balling threshold. The cap shape as calculated from Eqs. (9)–(12) for $n = 1$ and $n = 2$ is also included. In the normalized form, it can be seen that the ratio between the depth and width of the melt pool in the substrate is independent of the material properties and power as they are scaled by the same factor. The numerical value of the ratio is 0.23, as shown in [supplementary material 1](#).

2.4. The temperature field for thin welds

As the molten powder spreads over the substrate, the contact angle and the height of the melt decrease. If the melt track becomes thin enough, the thermal boundary condition will no longer be well approximated by Eq. (5). Instead, the boundary condition will begin to approximate the laser intensity distribution. As a first approximation, we assume that the heat transfer to the substrate is described by:

$$\left. \frac{\partial T}{\partial z} \right|_{z=0} = \begin{cases} -\frac{P\delta}{\pi r_l^2 k}, & |r| \leq r_l \\ 0, & |r| > r_l \end{cases} \quad (17)$$

which is similar to Eq. (5) but with the radius given by the laser spot radius, r_l .

The temperature distribution is:

$$T(r, z) = \frac{P\delta}{\pi r_l k} \int_0^\infty \frac{e^{-\lambda |z|} J_0(\lambda r) J_1(\lambda r_l)}{\lambda} d\lambda + T_0 \quad (18)$$

The wetted radius r_w is then given by:

$$T_M = T(r_w, 0) = \frac{P\delta}{\pi r_l k} \int_0^\infty \frac{J_0(\lambda r_w) J_1(\lambda r_l)}{\lambda} d\lambda + T_0 \quad (19)$$

which can be solved numerically for r_w .

2.5. Summary of the model assumptions

The key model assumptions are here summarized and discussed:

- The scanning speed is low, i.e. the ψ ratio is smaller than unity.
- The melt pool flow is neglected. In terms of heat transport, this implies that the thermal Péclet number, $Pe = \frac{u_L \rho_L c_{pL} d_L}{k_L}$, is small. Here, u_L is the characteristic liquid velocity in the melt pool, d_L the characteristic length, k_L the liquid thermal conductivity, ρ_L the liquid density, and c_{pL} the liquid specific heat. Geometrically, since r_w completely determines the melt pool shape in the model, the melt pool flow must be modest enough so that no liquid overflow beyond r_w occurs.
- The contact area between the molten cap and the metal substrate is assumed to be circular. In reality, the molten metal will oscillate and slosh around. In order for the assumption to still be valid, the average shape of molten cap footprint on the substrate must be close to a circle, with the time scale of the oscillation smaller than the heat diffusion time in the metal, so that the boundary condition (5) is quasi steady with respect to Eq. (4).

The legitimacy of these assumptions can be verified a posteriori, for typical LPBF conditions, by suitably designed CFD simulations, which are described in Section 3.2, and whose results are discussed in Section 4.2.

2.6. Extrapolation to higher scanning speeds

The analytical model neglects the scanning of the laser, but a qualitative understanding of the behavior at higher scanning speeds (i.e. higher ψ) can be reached by studying the Rosenthal problem. The Rosenthal problem considers, like the model presented in this paper, a semi-infinite substrate with a point heat source moving at speed u .

As shown for example in [23], the wetted radius will be given, at low relative scanning speeds ($\psi \ll 1$), by $r_w = \frac{P\delta}{4\pi\Delta T_m k}$, and at high scanning speeds ($\psi \gg 1$) by $r_w = \sqrt{\frac{2}{e} \frac{k}{u\rho c_p} \frac{P\delta}{\pi\Delta T_m k}}$. This can be rearranged using the wetting criterion for the balling threshold $r_w = 2.6r_p$ to:

$$P = \frac{(2.6)^2}{2} e\pi \frac{r_p \Delta T_m k}{\delta} \frac{u r_p \rho c_p}{k} = 1.13 P_{\text{balling}} \psi^* \quad (20)$$

where ψ^* is normalized by the powder radius instead of the laser spot size: $\psi^* = \frac{u r_p \rho c_p}{k}$. Therefore, at higher scanning speeds, we can expect the balling threshold to be linear with respect to the ψ^* number.

3. Experimental and numerical methods

3.1. Preparation and characterization of samples

Block-shaped samples of dimension $5 \times 5 \times 4 \text{ mm}^3$ were produced in a SISMA MySint 100 (SISMA, Italy) LPBF machine, equipped with a cw-fiber laser (wave length of 1070 nm). The laser spot is Gaussian with a $1/e^2$ diameter of 55 μm and a power adjustable from 20 to 200 W. The samples were fabricated from high conductivity oxygen free copper (Sandvik-Osprey, U.K.), bronze (Cu-6.7Sn-0.3Ni wt.-% of unknown origin), and 316 L Stainless Steel (Oerlikon Metco, Switzerland). The powders were sieved using a 45 μm sieve. All powders have a mean diameter close to 35 μm and are spherical in shape. The parts were made using a unidirectional scanning strategy so that any balling defects are clearly visible. The scanning speed was kept constant for every material and selected so that the different materials have approximately the same ψ number. The power was varied from 25 W to 200 W for bronze, 125–200 W for copper, and 20–50 W for steel. The hatch distance between adjacent scanning tracks was set to be significantly below the expected minimum balling diameter at 70 μm . For the top layer, a hatch distance of 300 μm

was used to facilitate the measurement of the wetting width. All parameters are summarized in Table 1.

The as-fabricated samples were cross-sectioned, mechanically ground and carefully polished with 50 nm alumina suspension to avoid smearing of pores. The samples were characterized by optical microscopy using a Leica Axiovert Metallographic Microscope (Leica, Germany). The wetting width of the top layer scans was measured manually using the Imagic IMS (Imagic Bildverarbeitung AG, Switzerland) image analysis software. To clearly see the melt boundaries of the steel samples, etching using V2A-etchant was necessary. The relative density of the samples was measured from the cross-sectional images using thresholding in FIJI [24].

3.2. Computational fluid dynamics simulations

To simulate the wetting process and to verify the model assumptions, a two-phase CFD code based on the OpenFOAM interFoam solver was developed. The OpenFOAM framework is described in detail by Weller et al. [25] and the interFoam solver is described and validated by Deshpande et al. [26].

The interFoam solver is a finite volume method (FVM), which uses the PIMPLE algorithm for solving the continuity and momentum conservation equations, and the volume of fluid (VOF) method for capturing the interface between the two phases. The phase fraction of metal is described with a scalar, ϕ , in every grid cell. The temporal evolution of the phase fraction is calculated based on its advection equation:

$$\frac{\partial \phi}{\partial t} = -\nabla \cdot (\mathbf{u}\phi) \quad (21)$$

The phase fraction of the gas is $(1 - \phi)$. In this framework, the fraction of liquid metal to total metal is calculated by thermodynamics and denoted by γ , and therefore the fractions of liquid metal and solid metal are $\gamma\phi$ and $(1-\gamma)\phi$ respectively. The fluid velocity, \mathbf{u} , and pressure field, p , are calculated from the momentum and continuity equations using the PIMPLE algorithm, which is described in [27].

The continuity equation for incompressible flow is given by $0 = \nabla \cdot \mathbf{u}$. The momentum equation is modified to include sources for the surface tension (S_σ), recoil pressure (S_R), and dampening D'Arcy force (S_D):

$$\frac{\partial \rho \mathbf{u}}{\partial t} = -\nabla \cdot (\rho \mathbf{u} \mathbf{u}) - \nabla p + \nabla \cdot (\mu \nabla \mathbf{u}) + S_\sigma + S_R + S_D \quad (22)$$

The density is evaluated per phase according to $\rho = \phi \rho_{\text{metal}} + (1-\phi)\rho_G$ using the value of ϕ from the last time step. The viscosity is calculated similarly: $\mu = \phi \mu_{\text{metal}}(T) + (1-\phi)\mu_{\text{gas}}$ where the viscosity of the metal is dependent on the metal phase $\mu_{\text{metal}} = \begin{cases} \mu_L, T > T_m \\ \mu_S, T < T_m \end{cases}$.

The surface tension contribution includes Marangoni convection:

Table 1

Parameters used for the manufactured cubes and the calculated dimensionless parameters ψ and Balling ratio (Ba). The samples marked with * were processed on a phosphor bronze base plate, all the others on a stainless steel base plate.

Material	Scanning speed (mm/s)	ψ	Power (W) / Ba			
			Sample 1	Sample 2	Sample 3	Sample 4
Cu	300	0.22	200 / 0.25	175 / 0.21	150 / 0.18	125 / 0.15
			200 / 1.65	175 / 1.45	150 / 1.24	125 / 1.03
Bronze	100	0.17	100 / 0.83	75 / 0.62	50 / 0.41	25 / 0.21
			200 / 1.65	175 / 1.45	150 / 1.24	125 / 1.03
Bronze*	100	0.17	200 / 50 / 2.07	175 / 40 / 1.66	150 / 30 / 1.24	125 / 20 / 0.83
Steel 316 L	20	0.29	50 / 2.07	40 / 1.66	30 / 1.24	20 / 0.83

$$S_\sigma = \left[\sigma_{LG} \kappa \mathbf{n} + \frac{\partial \sigma_{LG}}{\partial T} (\nabla T - \mathbf{n}(\mathbf{n} \cdot \nabla T)) \right] |\nabla \phi| \frac{2\rho}{\rho_L + \rho_G} \quad (23)$$

where σ_{LG} is the temperature dependent surface tension coefficient, the surface curvature is $\kappa = -\nabla \cdot \mathbf{n}$, and the interface normal is $\mathbf{n} = \frac{\nabla \phi}{|\nabla \phi|}$. The factor $\frac{2\rho}{\rho_L + \rho_G}$ redistributes the force to the metal and $|\nabla \phi|$ constrains it to the interface. The recoil pressure is calculated using the method presented in [28]:

$$S_R = -0.54 p_0 \exp\left(\frac{L_{vap} M (T - T_V)}{R T T_V}\right) \mathbf{n} |\nabla \phi| \quad (24)$$

where p_0 is the surrounding thermodynamic pressure, M the molar mass of the metal, T the local temperature, T_V the boiling point, L_{vap} the latent heat of vaporization, and R the universal gas constant.

To freeze the movement of the metal below the melting point a dampening term, which is large in the solid phase, is added:

$$S_D = \begin{cases} -DC \frac{(1-\gamma)^2}{\gamma^3 + \epsilon} \mathbf{u} & T < T_M \\ 0 & T > T_M \end{cases} \quad (25)$$

where γ is the fraction of liquid metal to metal in the grid cell: $\gamma = \min\left(1, \max\left(0, \frac{T - T_S}{T_L - T_S}\right)\right)$, T_L and T_S are the liquidus and solidus temperature respectively, ϵ is a small number, to avoid division by 0. The proportionality coefficient DC was set to 10^6 .

The temperature field is evolved according to the heat equation:

$$\frac{\partial \rho c_p T}{\partial t} = -\rho c_p \nabla \cdot (\mathbf{u} T) + \nabla \cdot (k \nabla T) + S_E + S_L \quad (26)$$

where S_E and S_L represent the evaporative cooling and laser heating, which will be expanded in later paragraphs.

The heat capacity is dependent on the phase:

$$c_p = \begin{cases} \phi c_p^s + (1-\phi) c_p^g & , T < T_S \\ \phi c_p^m + (1-\phi) c_p^g & , T_S < T < T_L \\ \phi c_p^l + (1-\phi) c_p^g & , T_L < T \end{cases} \quad (27)$$

where the heat capacity of the solid, liquid, and gas (c_p^s , c_p^l , and c_p^g respectively), as well as the effective heat capacity of the mushy zone, which includes the contribution of the latent heat of fusion: $c_p^m = \frac{L_{fus}}{T_L - T_S} + \frac{c_p^s + c_p^l}{2}$ are considered.

The thermal conductivity is calculated in a similar way:

$$k = \begin{cases} \phi k_s + (1-\phi) k_g & , T < T_S \\ \phi(1-\gamma) k_s + \phi \gamma k_L + (1-\phi) k_g & , T_S < T < T_L \\ \phi k_L + (1-\phi) k_g & , T_L < T \end{cases} \quad (28)$$

with k_s , k_L , and k_g the thermal conductivity of solid, liquid, and gas respectively.

The volumetric laser heat source, S_L , is calculated at every time step by generating discrete laser particles at the top boundary of the simulation domain, which carry power according to a Gaussian distribution, and are tracked in the Lagrangian sense through the domain. The generated particle has an initial power of

$$P_{\text{particle}} = \frac{2P}{\pi r_l^2} A_{\text{cell}} \exp\left(-\frac{2(x^2 + y^2)}{r_l^2}\right) \quad (29)$$

where A_{cell} is the area of the patch where the particle was generated. The particle is moved in increments smaller than the CFD cell size in the direction of the laser, \mathbf{d} . When the particle reaches a metal-gas interface cell, the heat source is incremented with the absorbed power

$$S_L^{\text{cell}} = S_L^{\text{cell}} + \frac{\alpha P_{\text{particle}}}{V_{\text{cell}}} \quad (30)$$

where α is the optical absorption coefficient, and the particle power is reduced by a corresponding amount:

$$P_{\text{particle}} = (1 - \alpha) P_{\text{particle}} \quad (31)$$

The direction is updated according to the law of reflection based on the surface normal at the interface:

$$\mathbf{d}_{\text{new}} = \mathbf{d}_{\text{old}} - 2(\mathbf{d}_{\text{old}} \cdot \mathbf{n}) \mathbf{n} \quad (32)$$

The particle continues propagating until it leaves the domain, or the power is less than $0.01 P_{\text{particle, initial}}$.

The evaporative cooling is calculated as a sink term, which corresponds to the recoil pressure in Eq. (22):

$$S_E = -\frac{0.82 L_{vap} P_0 M}{\sqrt{2\pi R T M}} \exp\left(\frac{L_{vap} M (T - T_V)}{R T T_V}\right) |\nabla \phi| \quad (33)$$

The simulated configuration consists of a stationary laser ($\psi = 0$) shining on top of a layer of bronze spherical particles. The computational domain is a box of size $600 \times 600 \times 500 \mu\text{m}^3$, discretized into mesh cells of $5 \times 5 \times 5 \mu\text{m}^3$. Only a quarter of the domain ($300 \times 300 \times 500 \mu\text{m}^3$) is simulated, as symmetry boundary conditions are imposed at $x = 300 \mu\text{m}$ and $y = 300 \mu\text{m}$. The boundary conditions on the non-symmetry faces are a fixed temperature of 300 K, no slip for the velocity field, and zero gradient for ϕ . One layer of $45 \mu\text{m}$ diameter powder was added on a flat substrate as a single tightly packed layer with lattice parameter (distance between the center-points of two adjacent particles) $50 \mu\text{m}$. The powder was chosen to have a diameter smaller than the lattice parameter to ensure that the powder particles remain thermally isolated from each other. For the same reason the powder particles were raised $5 \mu\text{m}$ from the substrate, except for the center particle. In this manner, the unmolten particles are separated from each other and from the substrate by one grid cell, which is filled by metal as soon as the melting starts, so that heat transfer between particles and between particles and substrate is only triggered when the particles reach the melting point. This aims at approximating the configuration illustrated in Fig. 3(a), where the unmolten particle contacts are tangential points with zero contact area, and the heat transfer happens when the molten cap is formed.

A sketch of the computational domain and configuration is presented in Fig. 6.

Due to the resolution and the decreased powder size, the volume of powder is 27% lower than a tightly packed bed. The simulation was performed using laser powers of 50 W, 100 W, 150 W, and 200 W, which correspond to balling ratios of 0.24, 0.49, 0.73, 0.97. All simulations ran for a simulated time of 500 ms using dynamic time steps. The material parameters used for the simulations are summarized in Table 2.

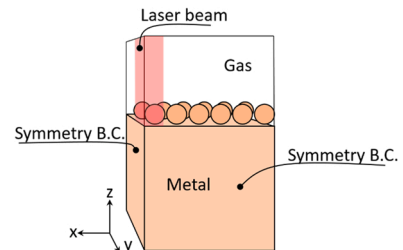


Fig. 6. Sketch of the computational domain.

Table 2

Model parameters used for the simulations.

	Property	Value	Unit	Notes
T_S	Solidus temperature	1153	K	Calculated for Cu-7Sn using [29]
T_L	Liquidus temperature	1306	K	Calculated for Cu-7Sn using [29]
T_V	Boiling temperature	2800	K	Value of copper
k	Thermal conductivity	77	W/m/K	Estimated from Nordheim's and Franz-Wiedeman's laws
M	Molar mass	65.5	g/mol	Standard values for Cu-6.7Sn-0.3Ni
c_p^s	Specific heat capacity, solid	425.6	J/kg/K	Calculated for Cu-7Sn using [29], as average from room temperature to solidus
c_p^l	Specific heat capacity, liquid	475.9	J/kg/K	Calculated for Cu-7Sn using [29], as average from liquidus to boiling temperature
c_p^G	Specific heat capacity, air	1010	J/kg/K	Standard value
L_{fus}	Latent heat of fusion	175.3	kJ/kg	Calculated for Cu-7Sn using [29]
L_{vap}	Latent heat of vaporization	451	kJ/kg	Calculated as simple mixture from standard data
σ_{LG}	Surface tension	1.4	N/m	For Cu-7Sn,[30]
$\frac{\partial \sigma_{LG}}{\partial T}$	Temperature coefficient for surface tension	0.16	mN/m/K	For Cu-7Sn,[30]
α	Absorption coefficient	0.4	u.l.	Free parameter
p_0	Surrounding pressure	10^5	Pa	Atmospheric pressure

4. Results and discussion

4.1. Comparison of the analytical model calculations with the experimental results

In the parts fabricated from bronze and steel, the low power samples show clear balling, which gradually transitions to lack-of-fusion porosity with increasing power. At high power the samples are nearly pore free. The transition from balling to conduction mode is shown for the bronze samples in Fig. 7, and is accompanied by a widening and flattening of the melt track. The corresponding for the steel and copper samples are available in [supplementary material 2](#).

For the copper samples, which all had a relative density around 73–75%, the power was too low to cover the transition. A tightly packed ideal powder bed has a relative density of 74%, which indicates that the

samples are close to being in incomplete melting mode. This hypothesis is further supported by the size of the balling features, which are typically around 70 μm . In some cases, they are as small as 35 μm , which indicates that uncoagulated powder is present.

Expressing the power in terms of the balling ratio allows the direct comparison of the results for the different materials. The fraction of laser power that is transferred to the solid substrate, δ , can be regarded as the leftover power from the heating and melting of the powder bed, taking into account thermal losses due to evaporation and radiative cooling. Therefore, if α_{eff} is the effective absorptivity of the powder bed (which includes the effect of multiple reflections and heat losses), and f is the fraction of the absorbed energy that goes into heating and melting the powder per unit time, then $\delta = \alpha_{eff}(1 - f)$. Both α_{eff} and f are difficult to measure experimentally due to the complexity of the laser-material interaction. Here, δ was selected as a free parameter. Good agreement with the experiments was found when $\delta_{Cu} = 0.14$, $\delta_{Bronze} = 0.18$ and $\delta_{316L} = 0.25$, as summarized in Table 3. Considering reported values for α_{eff} of copper and stainless steel powder of approximately 0.19 [31] and 0.32 [32], respectively, these values for δ appear to be reasonable as they are just below the values for α_{eff} , and imply that f is around 25% of α_{eff} .

The relationship between the balling ratio Ba , the relative density, the wetted diameter, and the pore morphology is shown in Fig. 8. The relative density is plotted as a function of the balling ratio. Two clear regions can be observed: below the balling threshold ($Ba = 1$) the density is increasing linearly, and above this value a plateau is reached. Least-square fitting of the data points (excluding the bronze samples with $Ba = 1.03$, which do not follow the trend) above and below the balling threshold yields two lines which intersect close to $Ba = 1$. Almost completely dense samples (>99.9%) are achieved above a balling ratio of 1.5. This corresponds, as shown in Fig. 3, to the height of the melt track being less than the powder diameter.

In Fig. 8(b), the wetted diameter is plotted as a function of the balling ratio together with the prediction by Eqs. (8) and (17). Once the threshold for balling is exceeded, the predicted diameters of the melt

Table 3

Model parameters for the materials used in the study.

Material	T_M	k	δ	$P_{balling}$
Cu	1356 K	370 W/m/K	0.14	759 W
Bronze	1306 K	77 W/m/K	0.18	121 W
316 L	1708 K	16 W/m/K	0.25	24 W

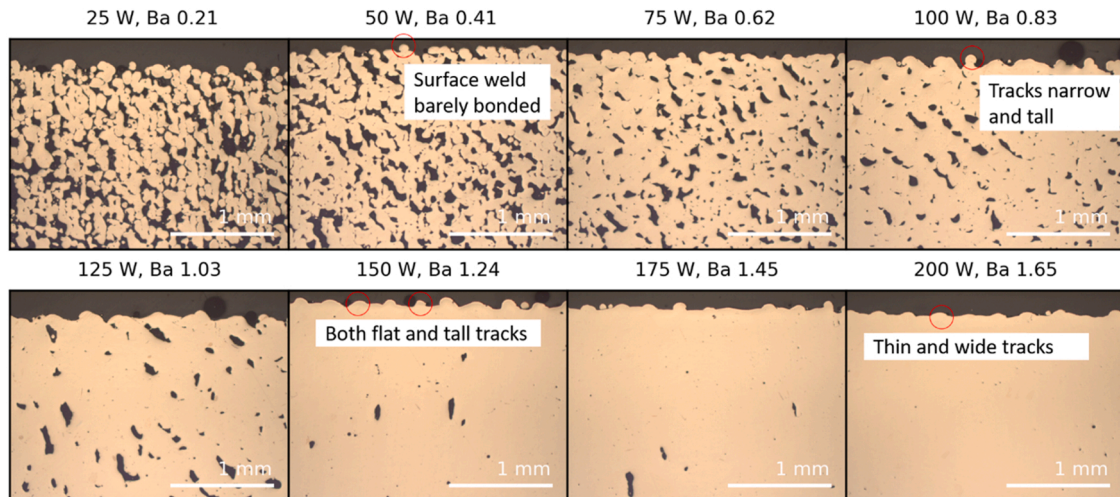


Fig. 7. Cross sections of the bronze samples processed at different power. As the power is increased the balling defects disappear and the weld tracks get wider and flatter.

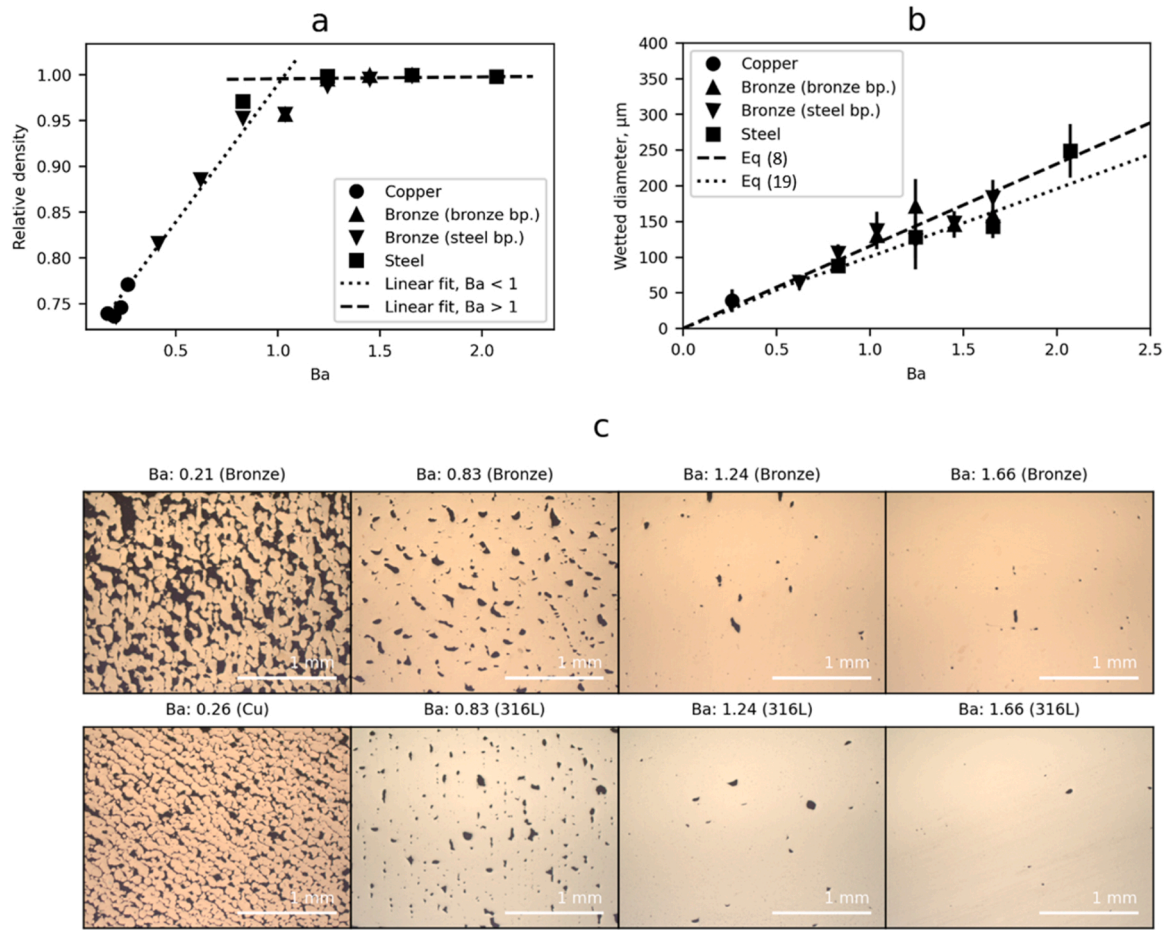


Fig. 8. The transition from balling to conduction mode expressed in terms of the balling ratio for the processed materials. (a) Relative density of the samples plotted against the balling ratio. The dotted and dashed lines are linear fits of the values below and above the balling threshold respectively. The two bronze data points right at the balling threshold were not included in the fit. (b) Average of the measured wetting diameter versus balling ratio. The solid line shows the 95% confidence interval of the mean. The values predicted by Eqs. (8) and (19) are overlaid. (c) Optical cross-sections showing that the pore morphology for different materials is similar at similar balling ratios.

tracks from Eq. (8) are often overestimations. The measured values are, however, in good agreement with the predictions according to Eq. (17), which is valid when the weld track is wide and shallow, approximating a plate weld. Depending on the local powder density, one would expect the wetting diameter to fluctuate as the melt is fluctuating between

including the second and third neighbor lines. This is indeed observed as a larger variance in the measured wetting widths around and above the balling threshold.

Despite the simplicity of the analytical model, the wetting radius values calculated by Eq. (17) are in good agreement with the

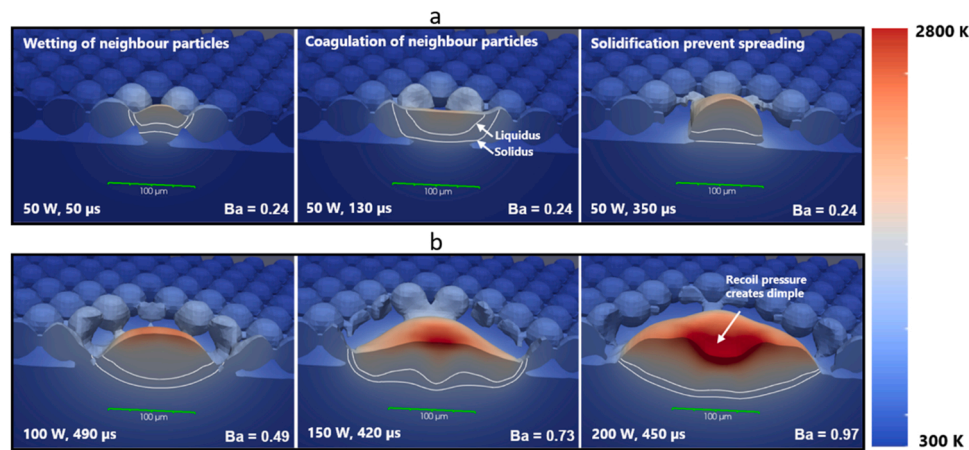


Fig. 9. Simulation of balling in bronze at different power, colored by temperature. (a) The process of wetting and coagulation of the neighbor powder particles, and the formation of a ball at 50 W power ($Ba = 0.24$). (b) The instantaneous shape at 100 W, 150 W, and 200 W power ($Ba = 0.49, 0.73, 0.97$). In all four cases it can be seen that the liquid spreading is constrained by the melt pool edge.

experimental values, which are measured from the top layer scanning tracks using *Imagic IMS*. Furthermore, the use of the balling ratio to normalize the power with materials properties is also useful for collapsing the relative density (measured from the cross-sectional images using FIJI) of all three materials into one curve. This, together with the similarity of the pore morphology for the different materials at similar values of Ba , indicates that the model describes the balling phenomenon reasonably well.

4.2. CFD results and verification of the model assumptions

The results from the CFD simulations at different laser powers for the bronze alloy are presented in Fig. 9. At 50 W ($Ba = 0.24$), the simulation shows a clear balling structure forming after 350 μ s. The melt does not penetrate into the substrate. At 100 W ($Ba = 0.49$), the melt pool penetrates into the substrate, and the penetration depth increases with increasing power. Close to the balling threshold, at a laser power of 200 W ($Ba = 0.97$), a depression starts to form on the melt pool surface, indicating the onset of keyhole formation.

The cap and melt pool are highly dynamic, and the cap sashes backward and forward on the substrate, as illustrated in Fig. 10 (a)–(c). This sloshing allows the melt pool to reach further into the powder bed than expected from the equilibrium position, showing why $n = 2$ in Eq. (10) is not sufficient to predict the balling threshold. As can be seen in both Figs. 9 and 10 (d) the melt pool edge in the substrate and the wetting radius coincide with each other. This shows that the assumption in the analytical model that the cap spreading is constrained by the melt pool edges is valid.

The thermal Péclet number can be estimated as $\overline{Pe} = \frac{2\overline{u}_L \rho_L c_{pL} r_p}{k_L}$, where the average liquid velocity magnitude \overline{u}_L is calculated from the simulation, and the characteristic length of heat conduction is taken as the powder diameter ($2r_p$), which approximates for all cases the molten cap height (the heat is dissipated through conduction in the vertical direction from the molten cap to the metal substrate). Table 4 shows that the thermal Péclet number is of $O(1)$ for all simulated powers, indicating that, while heat convection is present, it does not dominate the heat exchange compared to conduction. Therefore the Laplace Eq. (4) is a reasonable first order approximation of the heat transport, especially close to the contact area between the molten cap and the solid substrate, where the velocity is significantly smaller than \overline{u}_L ; while convection can be expected to be relevant mostly in the molten cap bulk and contribute to its thermal mixing.

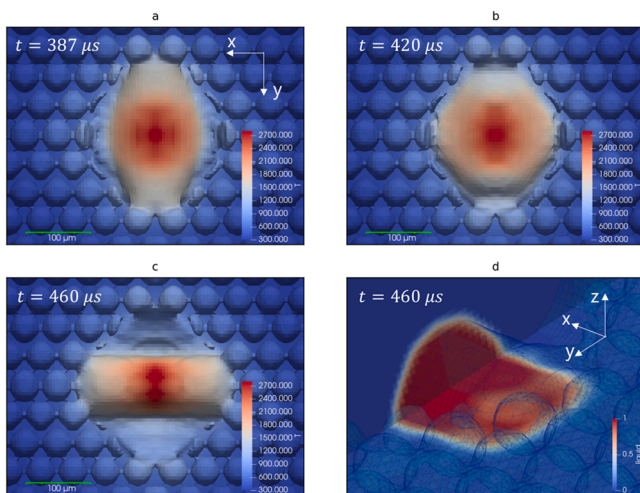


Fig. 10. Simulation of balling in bronze at 150 W laser power ($Ba = 0.73$). (a)–(c) shows the top view colored by temperature at different times, and (d) shows a sectioning of the cap colored by the liquid phase fraction with the metal surface superimposed.

Table 4

Average thermal Péclet number, and time scale of the melt pool sloshing relative to the thermal conduction time scale, for the simulation cases.

Power	Ba	\overline{Pe}	$\overline{\tau}_{slosh} / \tau_{cond}$
50 W	0.24	2.48	0.30
100 W	0.49	2.47	0.18
150 W	0.73	2.69	0.21
200 W	0.97	2.74	0.23

As shown in Fig. 10, the molten cap sloshing deforms the shape of the melt pool from the purely circular solution of the Laplace equation. The molten metal digs a nearly circular well in the solid substrate, while the cap oscillates inside it with a footprint of approximately elliptical shape, with the minor and major axes switching alternatively. The eccentricity e of the elliptical footprint is calculated from the simulation and shown in Fig. 11. It can be seen that the molten cap does in fact oscillate around an average shape that is nearly circular ($\bar{e} < 0.5$) for all cases close to the balling threshold. The oscillation period, $\overline{\tau}_{slosh}$, is estimated as the average time scale between the eccentricity troughs, as marked by the black dots in Fig. 11, which indicate the points in time when the footprint is almost a circle.

As the boundary condition (5) implies that the contact area between the molten cap and the solid substrate is a circle with constant radius r_w , the ratio $\overline{\tau}_{slosh} / \tau_{cond}$ must be smaller than unity, so that the melt oscillations around the circular shape are fast enough with respect to the heat conduction that the boundary condition (5) can be considered quasi steady with respect to Eq. (4). This is indeed the case, as shown in Table 4. The heat diffusion time scale is here estimated as $\tau_{cond} = \frac{4\rho_L c_{pL} r_p^2}{k_L}$.

It should be noted that, for the lowest laser power (50 W, $Ba = 0.24$), i.e. the regime where the most severe balling is expected, the melt pool oscillations are more chaotic, without a quasi-regular period, and the shape more inconsistent, as seen in Fig. 11; thus the estimations for \bar{e} and $\overline{\tau}_{slosh}$ begin to lose meaning in this regime. This indicates that the closer the conditions to the balling threshold $Ba = 1$, the better the analytical model approximates the heat transfer, while it starts to break down for $Ba \ll 1$, which is in fact the operating window that needs to be avoided in order to alleviate balling defects.

5. Conclusions

The formation of balling defects in laser power bed fusion of copper, bronze and stainless steel at low scanning speeds has been investigated, with a unique combination of experiments, simulations and theoretical modeling. It was found that the porosity of the samples due to balling defects can be correlated to one dimensionless parameter, the balling ratio Ba , which combines the powder size, the thermal conductivity of the material, the pre-heating of the substrate, and the fraction of power input reaching the solid substrate. The transition from balling mode to conduction mode occurs when $Ba = 1$. This dimensionless parameter can also be used to predict the width of the melt pool, which corresponds to the wetted area on the substrate. According to the thermal model, balling occurs when the wetted diameter is below 2.6 times the average powder diameter. The suggested mechanism for balling, used to derive the dimensionless number, is based on the assumption that the melt pool geometry is completely determined by conductive heat transfer toward the substrate, and the distance of liquid spreading is constrained by the width of the melt pool. These assumptions are valid at low to moderate laser scanning speeds, and when the balling ratio is close to the balling threshold ($Ba = 1$); they start to break down as $Ba \ll 1$, when the input power is insufficient for a complete melting of the material in the scan track (lack of fusion regime), and as $Ba \gg 1$, when convective heat transfer becomes important and balling defects are not a concern. The numerical simulations support the assumptions and the proposed mechanism for the operating range considered.

The results generalize the balling mechanism to different metals, and

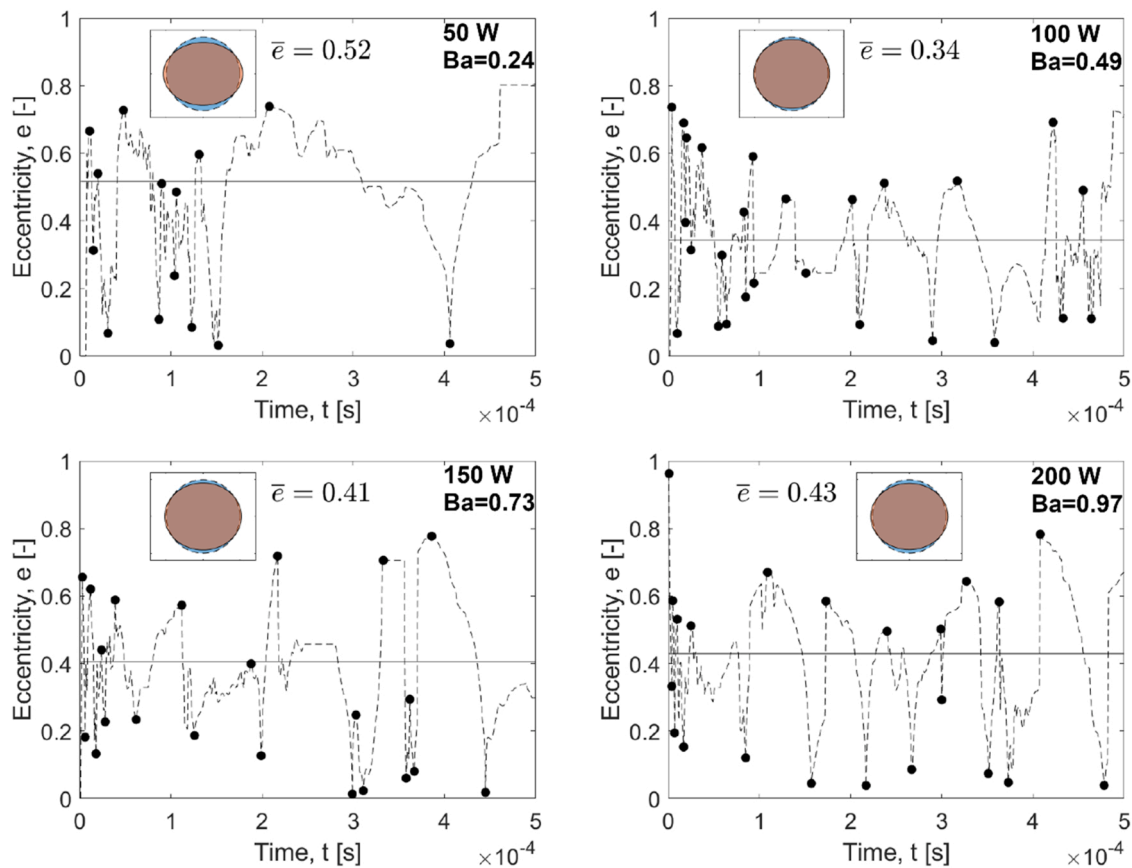


Fig. 11. Evolution of the melt pool footprint on the metal substrate. The footprint shape is approximated to an ellipse, and its eccentricity e is shown in time (dashed line), at different laser powers. The solid line shows the average eccentricity, around which the melt pool oscillates. The eccentricity peaks and troughs are marked by dots, to show the time scale and amplitude of the sloshing. The insets show the ellipse corresponding to the average eccentricity, compared to a circle ($e=0$) with the same area.

thus provide a strategy that can be used for alleviation of balling pores. In particular, the reduction of the powder size relative to the laser spot is identified as a good strategy, as it not only allows the manufacture of finer details, but can also be expected to widen the process window.

Future work will aim to further refine and generalize the balling model, with a more precise determination of the δ parameter, and extension to different regimes. In particular, having established that δ is proportional to the effective absorptivity of the powder bed α_{eff} for the balling regime, an exploration of the relation between α_{eff} and the optical absorptivity α in the balling regime will be carried out, by means of ray tracing simulations of the laser beam-powder bed interactions.

CRediT authorship contribution statement

Viktor Lindström: Conceptualization, Methodology, Software, Validation, Formal analysis, Investigation, Writing – original draft, Writing – review & editing, Visualization. **Giandomenico Lupo:** Conceptualization, Formal analysis, Investigation, Writing – original draft, Writing – review & editing. **Jian Yang:** Formal analysis, Writing – review & editing. **Vladyslav Turlo:** Methodology, Software, Writing – review & editing. **Christian Leinenbach:** Conceptualization, Writing – review & editing, Supervision, Resources, Project administration, Funding acquisition.

Declaration of Competing Interest

The authors declare that they have no known competing financial interests or personal relationships that could have appeared to influence the work reported in this paper.

Data availability

Data will be made available on request.

Acknowledgments

The work in this paper was funded through the PREAMPA project within the ETH Domain Special Research Focus Area (ETH-SFA) „Advanced Manufacturing“, Switzerland, which is gratefully acknowledged.

Competing interest

The authors declare no conflict of interest or competing interest.

Appendix A. Supporting information

Supplementary data associated with this article can be found in the online version at [doi:10.1016/j.addma.2023.103431](https://doi.org/10.1016/j.addma.2023.103431).

References

- [1] D.B. Hann, J. Iammi, J. Folkes, A simple methodology for predicting laser-weld properties from material and laser parameters, *J. Phys. D: Appl. Phys.* 44 (2011), <https://doi.org/10.1088/0022-3727/44/44/445401>.
- [2] W.E. King, H.D. Barth, V.M. Castillo, G.F. Gallegos, J.W. Gibbs, D.E. Hahn, C. Kamath, A.M. Rubenchik, Observation of keyhole-mode laser melting in laser powder-bed fusion additive manufacturing, *J. Mater. Process. Technol.* 214 (2014) 2915–2925, <https://doi.org/10.1016/j.jmatprotec.2014.06.005>.

- [3] A.M. Rubenchik, W.E. King, S.S. Wu, Scaling laws for the additive manufacturing, *J. Mater. Process. Technol.* 257 (2018) 234–243, <https://doi.org/10.1016/j.jmatprotec.2018.02.034>.
- [4] J. Ye, S.A. Khairallah, A.M. Rubenchik, M.F. Crumb, G. Guss, J. Belak, M. J. Matthews, Energy coupling mechanisms and scaling behavior associated with laser powder bed fusion additive manufacturing, *Adv. Eng. Mater.* 21 (2019) 1–9, <https://doi.org/10.1002/adem.201900185>.
- [5] S.A. Khairallah, A.T. Anderson, A. Rubenchik, W.E. King, Laser powder-bed fusion additive manufacturing: Physics of complex melt flow and formation mechanisms of pores, spatter, and denudation zones, *Acta Mater.* 108 (2016) 36–45, <https://doi.org/10.1016/j.actamat.2016.02.014>.
- [6] C. Zhao, K. Fezzaa, R.W. Cunningham, H. Wen, F. De Carlo, L. Chen, A.D. Rollett, T. Sun, Real-time monitoring of laser powder bed fusion process using high-speed X-ray imaging and diffraction, *Sci. Rep.* 7 (2017) 1–11, <https://doi.org/10.1038/s41598-017-03761-2>.
- [7] H. Ghasemi-Tabasi, J. Jhabvala, E. Boillat, T. Ivas, R. Drissi-Daoudi, R.E. Logé, An effective rule for translating optimal selective laser melting processing parameters from one material to another, *Addit. Manuf.* 36 (2020), 101496, <https://doi.org/10.1016/j.addma.2020.101496>.
- [8] M. Tang, P.C. Pistorius, J.L. Beuth, Prediction of lack-of-fusion porosity for powder bed fusion, *Addit. Manuf.* 14 (2017) 39–48, <https://doi.org/10.1016/j.addma.2016.12.001>.
- [9] E. Mirkoochi, D.E. Seivers, H. Garmestani, S.Y. Liang, Heat source modeling in selective laser melting, *Materials* 12 (2019) 1–18, <https://doi.org/10.3390/ma12132052>.
- [10] T.Q. Tran, A. Chinnappan, J.K.Y. Lee, N.H. Loc, L.T. Tran, G. Wang, V.V. Kumar, W.A.D.M. Jayatilaka, D. Ji, M. Doddamani, S. Ramakrishna, 3D printing of highly pure copper, *Metals* 9 (2019), <https://doi.org/10.3390/met9070756>.
- [11] F. Cooper, Sintering and additive manufacturing: the new paradigm for the jewelry manufacturer, *Proc. St. Fe Symp. . Jewel. Manuf. Technol.* (2012) 103–122.
- [12] D. Gu, Y. Shen, Balling phenomena during direct laser sintering of multi-component Cu-based metal powder, *J. Alloy. Compd.* 432 (2007) 163–166, <https://doi.org/10.1016/j.jallcom.2006.06.011>.
- [13] R. Li, J. Liu, Y. Shi, L. Wang, W. Jiang, Balling behavior of stainless steel and nickel powder during selective laser melting process, *Int. J. Adv. Manuf. Technol.* 59 (2012) 1025–1035, <https://doi.org/10.1007/s00170-011-3566-1>.
- [14] W. King, A.T. Anderson, R.M. Ferencz, N.E. Hodge, C. Kamath, S.A. Khairallah, Overview of modelling and simulation of metal powder bed fusion process at Lawrence Livermore National Laboratory, *Mater. Sci. Technol. (U. Kingd.)* 31 (2015) 957–968, <https://doi.org/10.1179/1743284714Y.0000000728>.
- [15] U.E. Klotz, D. Tiberto, F. Held, Additive manufacturing of 18-karat yellow- gold alloys, *Proc. St. Fe Symp. . Jewel. Manuf. Technol.* (2016) 255–272.
- [16] U.E. Klotz, D. Tiberto, F. Held, Optimization of 18-karat yellow gold alloys for the additive manufacturing of jewelry and watch parts, *Gold. Bull.* 50 (2017) 111–121, <https://doi.org/10.1007/s13404-017-0201-4>.
- [17] S.D. Jadhav, S. Dadbakhsh, L. Goossens, J.P. Kruth, J. Van Humbeeck, K. Vanmeensel, Influence of selective laser melting process parameters on texture evolution in pure copper, *J. Mater. Process. Technol.* 270 (2019) 47–58, <https://doi.org/10.1016/j.jmatprotec.2019.02.022>.
- [18] F. Klocke, C. Wagner, Coalescence behaviour of two metallic particles as base mechanism of selective laser sintering, *CIRP Ann. - Manuf. Technol.* 52 (2003) 177–180, [https://doi.org/10.1016/S0007-8506\(07\)60559-9](https://doi.org/10.1016/S0007-8506(07)60559-9).
- [19] Z. Mao, D.Z. Zhang, P. Wei, K. Zhang, Manufacturing feasibility and forming properties of Cu-4Sn in selective laser melting, *Materials* 10 (2017), <https://doi.org/10.3390/ma10040333>.
- [20] V. Lindström, O. Liashenko, K. Zweijacker, S. Derevianko, V. Morozovych, Y. Lyashenko, C. Leinenbach, Laser powder bed fusion of metal coated copper powders, *Materials* 13 (2020), <https://doi.org/10.3390/MA13163493>.
- [21] S.D. Jadhav, D. Fu, M. Deprez, K. Ramharter, D. Willems, B. Van Hooreweder, K. Vanmeensel, Highly conductive and strong CuSn0.3 alloy processed via laser powder bed fusion starting from a tin-coated copper powder, *Addit. Manuf.* 36 (2020), 101607, <https://doi.org/10.1016/j.addma.2020.101607>.
- [22] H.S. Carslaw, J.C. Jaeger, *Conduction of Heat in Solids*, 2nd ed., Oxford University Press, Oxford, 1959.
- [23] G. Wood, S. Al Islam, P.F. Mendez, Calibrated expressions for welding and ther application to isotherm width in a thick plate, *Soldag. e Insp.* 19 (2014) 212–220, <https://doi.org/10.1590/0104-9224/SI1903.03>.
- [24] J. Schindelin, I. Arganda-Carreras, E. Frise, V. Kaynig, M. Longair, T. Pietzsch, S. Preibisch, C. Rueden, S. Saalfeld, B. Schmid, J.Y. Tinevez, D.J. White, V. Hartenstein, K. Eliceiri, P. Tomancak, A. Cardona, Fiji: An open-source platform for biological-image analysis, *Nat. Methods* 9 (2012) 676–682, <https://doi.org/10.1038/nmeth.2019>.
- [25] H.G. Weller, G. Tabor, H. Jasak, C. Fureby, A tensorial approach to computational continuum mechanics using object-oriented techniques, *Comput. Phys.* 12 (1998) 620, <https://doi.org/10.1063/1.168744>.
- [26] S.S. Deshpande, L. Anumolu, M.F. Trujillo, Evaluating the performance of the two-phase flow solver interFoam, *Comput. Sci. Discov.* 5 (2012) 0–36, <https://doi.org/10.1088/1749-4699/5/1/014016>.
- [27] P.J. Oliveira, R.I. Issa, An improved PISO algorithm for the computation of buoyancy driven flows, *Numer. Heat. Transf.* (2001) 473–493.
- [28] K.Q. Le, C. Tang, C.H. Wong, On the study of keyhole-mode melting in selective laser melting process, *Int. J. Therm. Sci.* 145 (2019), <https://doi.org/10.1016/j.ijthermalsci.2019.105992>.
- [29] Thermo-Calc Software TCAL7 Al-based alloys database (accessed 2020–12-14), (n. d.).
- [30] J. Lee, W. Shimoda, T. Tanaka, Surface tension and its temperature coefficient of liquid Sn-X (X=Ag, Cu) alloys, *Mater. Trans.* 45 (2004) 2864–2870, <https://doi.org/10.2320/matertrans.45.2864>.
- [31] L. Gargalis, J. Ye, M. Strantz, A. Rubenchik, J.W. Murray, A.T. Clare, I.A. Ashcroft, R. Hague, M.J. Matthews, Determining processing behaviour of pure Cu in laser powder bed fusion using direct micro-calorimetry, *J. Mater. Process. Technol.* 294 (2021), 117130, <https://doi.org/10.1016/j.jmatprotec.2021.117130>.
- [32] J. Trapp, A.M. Rubenchik, G. Guss, M.J. Matthews, In situ absorptivity measurements of metallic powders during laser powder-bed fusion additive manufacturing, *Appl. Mater. Today* 9 (2017) 341–349, <https://doi.org/10.1016/j.apmt.2017.08.006>.